

# “Stop-and-go” error analysis of geosynchronous SAR

Yurun TIAN<sup>1,2\*</sup>, Shenglong GUO<sup>1,2</sup> & Weidong YU<sup>1</sup>

<sup>1</sup>*Institute of Electronics, Chinese Academy of Sciences, Beijing 100190, China;*

<sup>2</sup>*University of Chinese Academy of Sciences, Beijing 100190, China*

Received April 13, 2015; accepted May 27, 2015; published online September 29, 2015

**Abstract** In this paper, the slant range error introduced by the “stop-and-go” assumption is analyzed in detail. Owing to the high orbit and long synthetic aperture time of geosynchronous SAR (Geo-SAR), the slant range error introduced by the “stop-and-go” assumption should be considered. In addition, an accurate signal propagation delay time equation of Geo-SAR based on circle orbit is presented, and the error of the “stop-and-go” assumption is demonstrated by simulation. An “equivalent position” model is proposed and validated by simulation. The error of various powers of “stop-and-go” slant range is analyzed using Legendre orthogonal series expansion. The limitation of the stop-and-go assumption is proved by point target simulation.

**Keywords** geosynchronous SAR, stop-and-go assumption, equivalent position model, Legendre orthogonal series, error analysis

**Citation** Tian Y R, Guo S L, Yu W D. “Stop-and-go” error analysis of geosynchronous SAR. *Sci China Inf Sci*, 2016, 59(6): 062306, doi: 10.1007/s11432-015-5388-5

## 1 Introduction

Synthetic aperture radar (SAR) can work day and night regardless of weather conditions, and it has been developed remarkably during the past few decades. Currently, airborne and spaceborne SAR systems have been widely utilized in civil and military remote sensing missions, providing manifold unique information that is not available through other methods. The concept of geosynchronous SAR (Geo-SAR) was proposed in 1978 by Tomiyasu [1], and it soon drew the attention of the whole SAR domain. Compared to low-orbit SAR (Leo-SAR), Geo-SAR works on a much higher orbit of 36000 km, which reduces the revisit time of Geo-SAR to 24 h and increases the observation swath significantly. In the future, Geo-SAR will play an important role in disaster monitoring or even forecasting [2–4]. Despite its advantages, there are certain difficulties in realizing a feasible SAR system in geosynchronous orbit. In this paper, we focus on the imaging model analysis.

The “stop-and-go” assumption has been widely applied to the imaging geometry of Leo-SAR and airborne SAR [5]. Most satellite beam steering methods are based on this assumption [6], and the problem has been discussed in detail. The assumption is that the satellite transmits and receives the signal pulse at a stationary point, which means that all movements between and within the signal pulse are ignored [7, 8]. In Geo-SAR, the orbit height increases by two orders of magnitude compared to that

\* Corresponding author (email: leonbel@163.com)

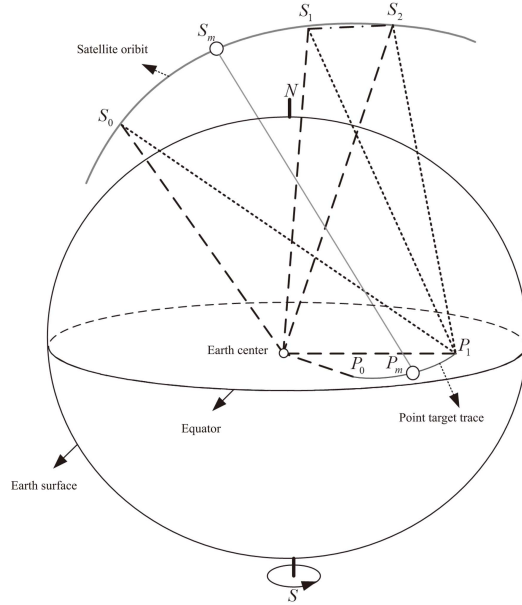


**Figure 1** Geometry structure of Geo-SAR.

of Leo-SAR. Therefore, the signal propagation delay time also increases by two orders of magnitude, so the relative movement during the signal propagation delay time should be considered [9]. Because the satellite velocity decreases notably and the resolution of Geo-SAR is usually at the meter level, the movements within a signal pulse could be ignored. Moreover, the angular velocity of the satellite is identical to the earth's rotational velocity, so the effect of the earth's rotation should be considered. The synthetic aperture time of Geo-SAR may reach hundreds of seconds, which means that the error caused by the "stop-and-go" assumption could be large.

This paper is organized as follows. Geo-SAR geometry structure and the "equivalent position" model are presented in Section 2. The errors of the conventional "stop-and-go" assumption and simulation experiment are given in Section 3, followed by the error analysis in Section 4. Section 5 presents the feasibility of the equivalent position model using point target simulation. Finally, conclusions are drawn in Section 6.

## 2 The geometry structure and signal model

The geometry structure of Geo-SAR is shown in Figure 1. The satellite moves a circular orbit with angular velocity  $\omega_s$ , and the point target moves along its latitude circle as the earth rotates with angular velocity  $\omega_e$ . Because the satellite is in geosynchronous orbit, we suppose that  $\omega_s = \omega_e$ . The satellite transmits a chirp signal at position  $S_0$ . At the same time, the point target is at position  $P_0$ . After the propagation time  $\tau_t$ , the transmitted signal impinges on the target at position  $P_1$ , and the satellite moves to position  $S_1$ . The signal reflects from the target immediately and then reaches the satellite after propagation time  $\tau_r$  at position  $S_2$ . Position  $S_m$  represents the midpoint of the satellite trajectory between  $S_0$  and  $S_2$ , and position  $P_m$  represents the midpoint of the point target movement trace between  $P_0$  and  $P_1$ .

To deduce the accurate propagation delay time, two right-handed coordinate systems are needed. One is the earth's inertial coordinate system  $E_o$ , and the other is the satellite orbit coordinate system  $E_v$ . The origin of  $E_o$  is located at the earth's center with its  $X$  axis pointing toward the vernal equinox and its  $Y$  axis pointing toward the north pole. The origin of  $E_v$  is located at the earth center with its  $X$  axis pointing toward the perigee and its  $Z$  axis vertical to the orbit plane. These two coordinate systems can

convert between each other through conversion matrix  $M_{ov}$ , which can be given as

$$M_{ov} = U_1(\theta)U_2(\eta)U_3(\alpha), \quad (1)$$

$$U_1(\theta) = \begin{bmatrix} \cos \theta & -\sin \theta & 0 \\ \sin \theta & \cos \theta & 0 \\ 0 & 0 & 1 \end{bmatrix},$$

$$U_2(\eta) = \begin{bmatrix} 1 & 0 & 0 \\ 0 & \cos \eta & -\sin \eta \\ 0 & \sin \eta & \cos \eta \end{bmatrix}, \quad (2)$$

$$U_3(\alpha) = \begin{bmatrix} \cos \alpha & -\sin \alpha & 0 \\ \sin \alpha & \cos \alpha & 0 \\ 0 & 0 & 1 \end{bmatrix},$$

where  $\theta$  is the longitude of the ascending node,  $\eta$  is the orbit inclination angle, and  $\alpha$  is the augment of perigee. The relationship between  $E_o$  and  $E_v$  can be given as

$$E_o = M_{ov}E_v, E_v = M_{ov}^T E_o, \quad (3)$$

where the superscript T stands for the matrix transpose.

Within the two coordinate systems, we can define the position vectors above as

$$\begin{cases} S_0^{E_o} = (s_{x0} \ s_{y0} \ s_{z0})^T, \\ S_1^{E_v} = (s_{x1} \ s_{y1} \ s_{z1})^T, \\ S_2^{E_v} = (s_{x2} \ s_{y2} \ s_{z2})^T, \\ P_0^{E_o} = (p_{x0} \ p_{y0} \ p_{z0})^T, \\ P_1^{E_o} = (p_{x1} \ p_{y1} \ p_{z1})^T, \end{cases} \quad (4)$$

where the superscript of each vector represents the coordinate system it is in. The earth model in  $E_o$  can be given as

$$\frac{x^2}{R_e^2} + \frac{y^2}{R_e^2} + \frac{z^2}{R_p^2} = 1, \quad (5)$$

where  $R_e = 6378.137$  km,  $R_p = 6356.752$  km.

Owing to the uniform circular motion of the satellite in circular orbit and the point target on its latitude circle, within any coordinate system, we can have

$$\begin{cases} \angle S_0 O S_1 = \omega_s \tau_t, \\ \angle S_1 O S_2 = \omega_s \tau_r, \\ \angle P_0 O P_1 = \omega_e \tau_t. \end{cases} \quad (6)$$

Within  $E_o$ , the point target rotates around the Z axis on its latitude plane, so after propagation delay  $\tau_t$ , we have

$$P_1^{E_o} = \begin{bmatrix} \cos(\omega_e \tau_t) & -\sin(\omega_e \tau_t) & 0 \\ \sin(\omega_e \tau_t) & \cos(\omega_e \tau_t) & 0 \\ 0 & 0 & 1 \end{bmatrix} P_0^{E_o}. \quad (7)$$

By substituting (4) into (7), we can get

$$P_1^{E_o} = \begin{bmatrix} p_{x0} \cos(\omega_e \tau_t) - p_{y0} \sin(\omega_e \tau_t) \\ p_{x0} \sin(\omega_e \tau_t) + p_{y0} \cos(\omega_e \tau_t) \\ p_{z0} \end{bmatrix}. \quad (8)$$

By applying cosine law to the triangle  $S_0P_0P_1$ , we can have the equation written as

$$\|P_0S_0\|^2 + \|P_0P_1\|^2 - 2 \langle S_0P_0, P_0P_1 \rangle = \|S_0P_1\|^2, \quad (9)$$

where the operator  $\|\cdot\|$  stands for norm, and  $\langle \cdot, \cdot \rangle$  stands for inner products. Then the equation of propagation delay  $\tau_t$  can be obtained

$$c^2\tau_t^2 + K_1 \sin(\omega_e\tau_t) + K_2 \cos(\omega_e\tau_t) + K_3 = 0, \quad (10)$$

where  $c$  is the speed of light, and

$$\begin{aligned} K_1 &= 2(p_{x0}s_{y0} - p_{y0}s_{x0}), \\ K_2 &= 2[r_t^2 + p_{x0}(s_{x0} - p_{x0}) + p_{y0}(s_{y0} - p_{y0})], \\ K_3 &= -s_{x0}^2 + p_{x0}^2 - s_{y0}^2 + p_{y0}^2 - (s_{z0} - p_{z0})^2 - 2r_t^2, \\ r_t &= \|P_0\| \cos \theta_{1at}, \end{aligned} \quad (11)$$

where  $\theta_{1at}$  and  $r_t$  are the latitude and the semi-diameter of the latitude circle at which the point target is located. Through (10) and (11),  $r_t$  can be solved numerically with sufficient precision. Moreover, within  $E_v$ , the satellite rotates around the  $Z$  axis on the orbit plane, so we can have

$$S_1^{E_v} = \begin{bmatrix} \cos(\omega_e\tau_t) & -\sin(\omega_e\tau_t) & 0 \\ \sin(\omega_e\tau_t) & \cos(\omega_e\tau_t) & 0 \\ 0 & 0 & 1 \end{bmatrix} S_0^{E_v}, \quad (12)$$

$$S_2^{E_v} = \begin{bmatrix} \cos(\omega_e\tau_r) & -\sin(\omega_e\tau_r) & 0 \\ \sin(\omega_e\tau_r) & \cos(\omega_e\tau_r) & 0 \\ 0 & 0 & 1 \end{bmatrix} S_1^{E_v}. \quad (13)$$

Using cosine law to the triangle  $S_2S_1P_1$ , we can get equation written as

$$\|S_1P_1\|^2 + \|S_1S_2\|^2 - 2 \langle S_1P_1, S_1S_2 \rangle = \|P_1S_2\|^2. \quad (14)$$

By now, the equation of propagation delay  $\tau_r$  can be obtained

$$c^2\tau_r^2 + L_1 \sin(\omega_e\tau_r) + L_2 \cos(\omega_e\tau_r) + L_3 = 0, \quad (15)$$

where

$$\begin{aligned} L_1 &= 2(p_{y1}s_{x1} - p_{x1}s_{y1}), \\ L_2 &= 2[r_s^2 + s_{x1}(p_{x1} - s_{x1}) + s_{y1}(p_{y1} - s_{y1})], \\ L_3 &= -p_{x1}^2 + s_{x1}^2 - p_{y1}^2 + s_{y1}^2 - (p_{z1} - s_{z1})^2 - 2r_t^2, \\ r_t &= \|S_0\|. \end{aligned} \quad (16)$$

Also, whereby (15), (16) can be solved numerically with sufficient precision. The overall propagation delay  $\tau_d$  can be easily calculated as  $\tau_d = \tau_t + \tau_r$ .

### 3 Error introduced by the “stop-and-go” assumption

The “stop-and-go” model assumes that the satellite and the point target are both at stationary points, which means that the model uses the slant rang between  $S_0$  and  $P_0$  to calculate the propagation delay. The movement between the signal transmission and reception is ignored. Let the angular velocity of both the satellite and the earth be 0. Eqs. (14) and (15) can be rewritten as

$$\begin{cases} c^2\tau_t^2 + K_2 + K_3 = 0, \\ c^2\tau_r^2 + L_2 + L_3 = 0, \end{cases} \quad (17)$$

**Table 1** Parameters of the simulation

Specifications	Value	Unit
Orbit semimajor axis	42164	km
Orbit eccentricity	0	
Orbit inclination	56	°
Perigee argument	0	°
PRF	204	Hz
Wavelength	0.24	m
Look angle	4.5	°

and we have

$$\begin{cases} S_0^{E_o} = S_1^{E_o} = S_2^{E_o}, \\ P_0^{E_o} = P_1^{E_o}. \end{cases} \quad (18)$$

As a result, Eq. (17) can be solved as

$$\begin{cases} \tau_t = \frac{\sqrt{(s_{x0} - p_{x0})^2 + (s_{y0} - p_{y0})^2 + (s_{z0} - p_{z0})^2}}{c}, \\ \tau_r = \frac{\sqrt{(s_{x0} - p_{x0})^2 + (s_{y0} - p_{y0})^2 + (s_{z0} - p_{z0})^2}}{c}. \end{cases} \quad (19)$$

Now we can see that the “stop-and-go” model is just a degradation form of the accurate propagation delay equation.

The simulation parameters are listed in Table 1. In the simulation, we use yaw steering method given by (20) to make sure the doppler center under “stop-and-go” assumption to be 0. The yaw angle  $\theta_y$  can be written as

$$\theta_y = -\arctan\left(\frac{\sin i \cos(f + w)}{\omega_s/\omega_e - \cos i}\right), \quad (20)$$

where  $f$  stands for true anomaly,  $w$  stands for argument of perigee,  $\omega_s$  is the satellite angular velocity,  $\omega_e$  is the earth’s rotational angular velocity, and  $i$  is the orbit inclination. Considering the long synthetic aperture time, the coupling of range/azimuth in the two-dimensional (2-D) signal will be so serious that small errors in Doppler parameters can lead to huge slant range errors. Attitude steering is an efficient technology to reduce the coupling of range/azimuth.

Through numerical calculation of the propagation delay for every position on the orbit, we can obtain the slant range difference between the accurate model and “stop-and-go” model. Here, we use a maximum synthetic aperture time of 1000 s.

Seen from Figure 2, we can find that “stop-and-go” assumption error (double way) reaches 4 m and increases with the synthetic aperture time. Hence, we must consider the error of the “stop-and-go” assumption in the image processing of Geo-SAR, when high resolution is required.

However, we can not distinguish the linear and nonlinear ingredients of the overall error. To determine the nonlinear error inside the overall error, equations must be found to fit the numerical range history under both “stop-and-go” and under accurate geometry. Here we use the polynomial fitting based on the Doppler parameters proposed in [10]. To ensure accuracy, we deploy six orders of Doppler parameters. Thus, the numerical range history can be replaced by a polynomial expressed as

$$R(\eta) = R_c + \sum_{n=1}^6 k_n(\eta - \eta_c)^n, \quad (21)$$

where  $\eta$  is the azimuth time,  $R_c$  is the slant range of the beam center crossing time  $\eta_c$ , and we have

$$\begin{cases} k_1 = V_c, k_2 = \frac{1}{2}A_c, k_3 = \frac{1}{6}B_c, \\ k_3 = \frac{1}{24}C_c, k_5 = \frac{1}{100}D_c, k_6 = \frac{1}{120}E_c, \end{cases} \quad (22)$$

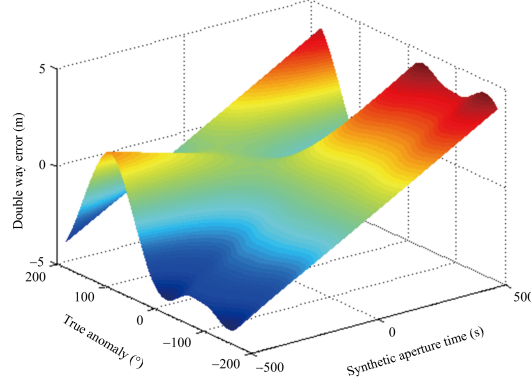


**Figure 2** (Color online) “Stop-and-go” error of the point targets in beam center all over the orbit.

where  $V_c, A_c, B_c, C_c, D_c, E_c, F_c$  represent the relative velocity and the first to fourth order relative acceleration rates. These movement parameters can be expressed as

$$\begin{cases} V_c = -\frac{\lambda}{2}f_{dc}, A_c = -\frac{\lambda}{2}f_{1r}, B_c = -\frac{\lambda}{2}f_{2r}, \\ C_c = -\frac{\lambda}{2}f_{3r}, D_c = -\frac{\lambda}{2}f_{4r}, E_c = -\frac{\lambda}{2}f_{5r}, \end{cases} \quad (23)$$

here, all the Doppler parameters can be evaluated according to the equation proposed in [10]. The expression of the echo in the 2-D frequency domain can be written as

$$S(f_t, f_r) = A_1 W_r(f_t) W_a(f_\eta - f_{\eta_c}) \exp\{j\varphi(f_t, f_\eta)\}, \quad (24)$$

where  $A_1$  is a complex constant,  $W_r(f_t)$  is the range frequency envelope, and  $W_a(f_\eta)$  is the azimuth frequency envelope. According to [11,12], we can have

$$\varphi(f_t, f_\eta) = -\frac{\pi f_t^2}{K_r} - \frac{4\pi(f_0 + f_t)}{c} R_c \sum_{n=1}^5 \frac{A_n}{n+1} M^{n+1}, \quad (25)$$

where  $f_0$  is Doppler center frequency, and

$$\begin{cases} M = -\left(\frac{c f_\eta}{2(f_0 + f_\eta)}\right) - V_c, \\ A_1 = \frac{1}{k_2}, A_2 = -\frac{k_3}{k_2^3}, A_3 = \frac{2k_3^2 - k_3 k_5}{k_2^5}, \\ A_4 = \frac{1}{k_2^7} (k_2 k_3 k_4 - k_2^2 k_5 - 5k_3^3), \\ A_5 = \frac{1}{k_2^9} (6k_2^2 k_3 k_5 + 3k_2^2 k_4^2 + 14k_3^4 - k_2^3 k_6 - 21k_2 k_3^2 k_4). \end{cases} \quad (26)$$

Again, in Figure 1, if we assume that at time  $\eta_c$  the satellite is at position  $S_0$  and the point target on the earth’s surface is at position  $P_0$ , then all orders of the Doppler parameters needed by range history under “stop-and-go” can be calculated at positions  $S_0$  and  $P_0$ .

The difference between the numerical and polynomial forms of the range history can be seen in Figure 3.

As shown in Figure 3(a), the polynomial fitting is efficient in 1000 s, so we can use it as the range history equation in the discussion below.

Because the numerical range history derived from the “equivalent position” model is sufficiently accurate, all we must do is to calculate the parameters required for the polynomial fitting of the range history under the equivalent position model. To achieve this, we can use satellite position  $S_m$  and target

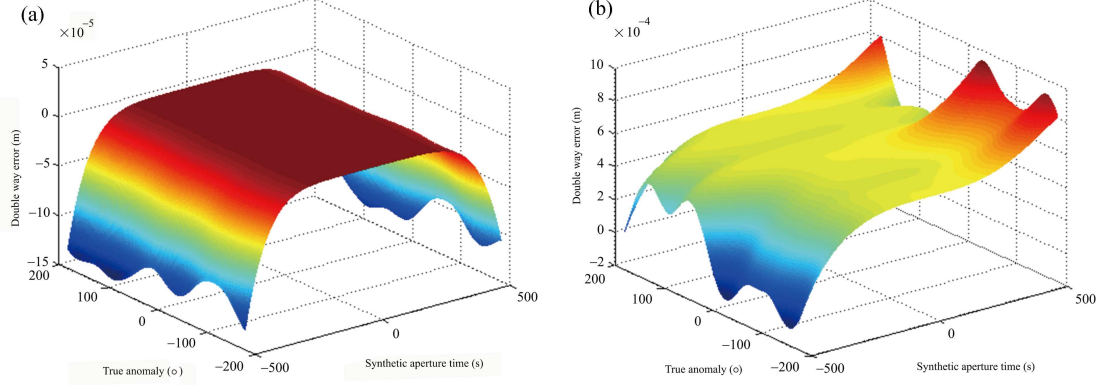


**Figure 3** (Color online) Sixth-order polynomial fitting error of the numerical range history under (a) “stop-and-go” assumption, and (b) accurate geometry.

position  $P_m$ . The difference between accurate numerical range history and the polynomial equation of the “equivalent position” model is shown in Figure 3(b).

From Figure 3(b), we can safely draw the conclusion that the accurate slant range history can be well represented by the sixth-order polynomial equation.

According to the geometry relationship in Figure 1, we can obtain the following expressions based on the cosine theorem

$$\begin{cases} \|S_0P_0\| = \sqrt{H_s^2 + R_t^2 - 2H_sR_t \cos \angle S_0OP_0}, \\ \|S_0P_1\| = \sqrt{H_s^2 + R_t^2 - 2H_sR_t \cos \angle S_0OP_1}, \\ \|S_2P_1\| = \sqrt{H_s^2 + R_t^2 - 2H_sR_t \cos \angle S_2OP_1}, \\ \|S_mP_m\| = \sqrt{H_s^2 + R_t^2 - 2H_sR_t \cos \angle S_mOP_m}, \end{cases} \quad (27)$$

where  $H_s$  is the satellite height, and  $R_t$  denotes the distance between the point target and the earth’s core.  $H_s$  and  $R_t$  are two constants. It is obvious that  $\angle S_0OP_0$  increases with the synthetic aperture time without any constraints. When  $\angle S_0OP_0 \leq \min(S_0OP_1, S_2OP)$  or  $\angle S_0OP_0 \geq \max(S_0OP_1, S_2OP)$ , the “stop-and-go” model will lose its effect. However, the inequity  $\min(S_0OP_1, S_2OP) \leq \angle S_mOP_m \leq \max(S_0OP_1, S_2OP)$  is always satisfied, which means that the error of “equivalent position” model will never be too large.

#### 4 Error analysis

The slant range equation discussed above is based on a finite Taylor series. Hence, every power Taylor series error can be expressed by

$$\begin{cases} T_{e0} = (R_{cm} - R_{csg}), T_{e1} = (V_{cm} - V_{csg})\eta, \\ T_{e2} = \frac{1}{2}(A_{cm} - A_{csg})\eta^2, T_{e3} = \frac{1}{6}(B_{cm} - B_{csg})\eta^3, \\ T_{e4} = \frac{1}{24}(C_{cm} - C_{csg})\eta^4, T_{e5} = \frac{1}{120}(D_{cm} - D_{csg})\eta^5, \\ T_{e6} = \frac{1}{720}(E_{cm} - E_{csg})\eta^6, \end{cases} \quad (28)$$

where subscript csg denotes the fitting parameters under the “stop-and-go” assumption, and subscript cm denotes the fitting parameters of the “equivalent position” model.

Overall error can be expressed as

$$T_{et}(\eta) = R_m(\eta) - R_{sg}(\eta), \quad (29)$$

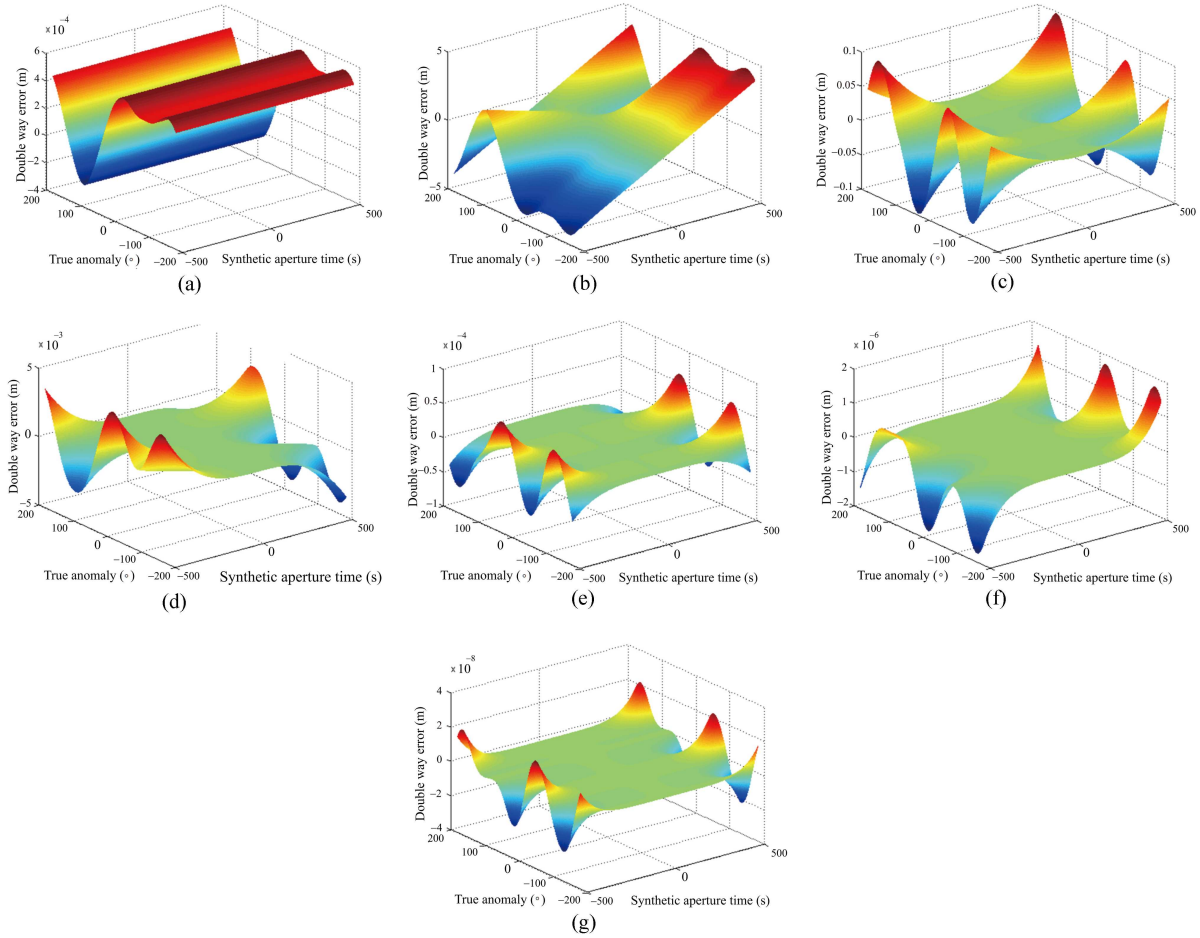


**Figure 4** (Color online) Power error based on Taylor series. (a) Constant error; (b) linear error; (c) quadratic error; (d) cubic error; (e) quartic error; (f) quintic error; (g) sextic error.

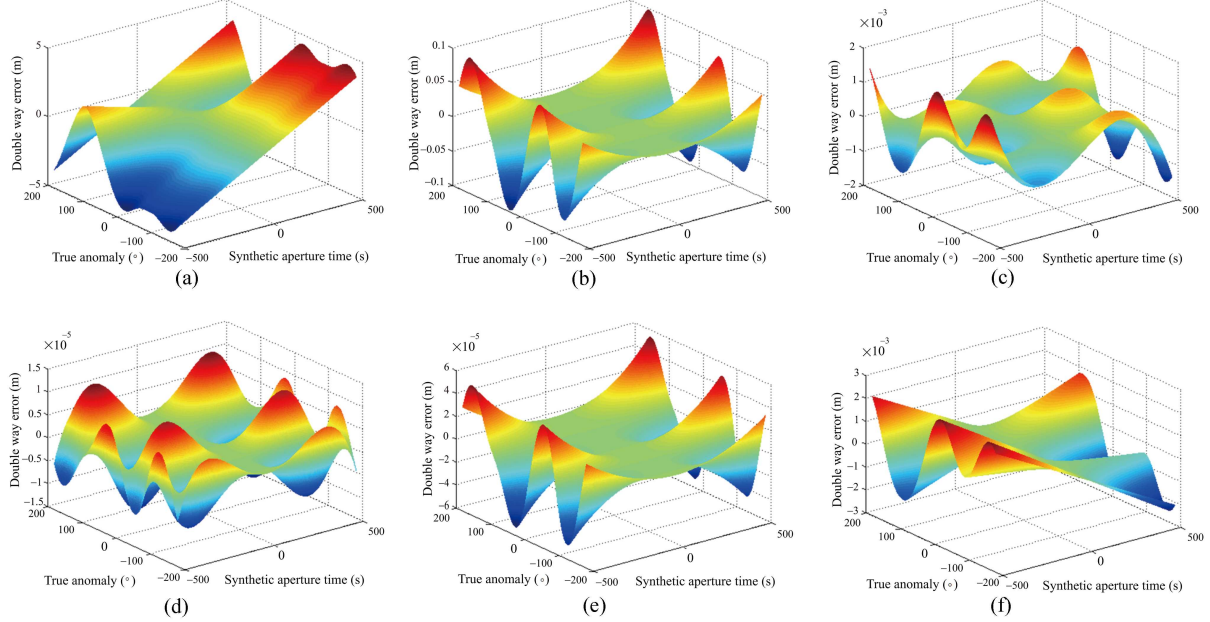
and each power error all over the orbit period is shown in Figure 4.

Figure 4 shows that there are constant errors produced by the difference of the slant range at the beam center crossing time of the point targets, linear error produced by the Doppler center error, and higher-order error produced by the error of other Doppler parameters. Among these errors, linear error is the most prominent. At the same time, nonlinear error will rise continuously with increasing synthetic aperture time. When synthetic aperture time reaches 1000 s, quadratic Taylor series error is up to 0.1 m, and the cubic Taylor series error arrives at  $10^{-3}$  m. However, besides these errors, others can be ignored.

However, we must note that the above error analysis based on Taylor series cannot accurately reflect the impact of slant range error on point target focusing. When slant range error that is more than quadratic cannot be neglected, the error analysis based on the Taylor series expansion will bring about significant disadvantages. We cannot accurately analyze the impact of power error on the azimuth pulse compression, owing to the coupling among both odd powers and even powers. Taylor series are not orthogonal. For example, the cubic and quintic Taylor series errors will also contribute to the Doppler center error, and the quintic and sextic Taylor series errors will also add to Doppler frequency rate error.

To exclude the possible coupling introduced by Taylor series, it is necessary to analyze the effect of each power error on the point target focus independently. Thus, we apply the Legendre orthogonal series to the orthogonal slant range equation.

Because the quintic and sextic Taylor series errors are rather small, we deploy only the Legendre series up to the fourth degree, which can be expressed as



**Figure 5** (Color online) Power error based on Legendre series. (a) Linear error; (b) quadratic error; (c) cubic error; (d) quartic error, and Coupling within Taylor series error; (e) quadratic error within quartic error; (f) linear error within cubic error.

$$\begin{cases} P_0(\eta) = \sqrt{\frac{1}{T_a}}, \\ P_1(\eta) = \sqrt{\frac{3}{T_a}} \left( \frac{2}{T_a} \eta \right), \\ P_2(\eta) = \sqrt{\frac{5}{T_a}} \left( \frac{6}{T_a^2} \eta^2 - \frac{1}{2} \right), \\ P_3(\eta) = \sqrt{\frac{7}{T_a}} \left( \frac{20}{T_a^3} \eta^3 - \frac{3}{T_a} \eta \right), \\ P_4(\eta) = \sqrt{\frac{9}{T_a}} \left( \frac{70}{T_a^4} \eta^4 - \frac{15}{T_a^2} \eta^2 + \frac{3}{8} \right), \end{cases} \quad -\frac{T_a}{2} \leq \eta \leq \frac{T_a}{2}, \quad (30)$$

where  $T_a$  stands for synthetic aperture time. And we have

$$\int_{-\frac{T_a}{2}}^{\frac{T_a}{2}} P_i(\eta) P_j(\eta) d\eta = \begin{cases} 0 & i \neq j; \\ 1 & i = j. \end{cases} \quad (31)$$

Consequently,  $T_{et}$  can be divided by

$$T_{et}(\eta) = K_0 P_0(\eta) + K_1 P_1(\eta) + K_2 P_2(\eta) + K_3 P_3(\eta) + K_4 P_4(\eta), \quad (32)$$

where

$$K_i = \int_{-\frac{T_a}{2}}^{\frac{T_a}{2}} T_{et}(\eta) P_i(\eta) d\eta \quad (i = 0, 1, 2, 3, 4). \quad (33)$$

Because the constant error has no effect on azimuth focusing, double-way slant range error from linear to quantic based on Legendre series is shown in Figure 5.

According to Figure 5(a)~(d), we note that there is coupling between quadratic and quartic error in original Taylor series. After orthogonal decomposition, the quartic error decreases, and quadratic error increases. In addition, there is also coupling between linear and cubic error in the original Taylor series.

**Table 2** Parameters of simulation

	Doppler bandwidth (Hz)	Beam footprint velocity (m/s)	Theoretical resolution (m)
PT2	170.77	384.63	1.995
PT0	168.26	381.53	2.009
PT1	165.68	378.30	2.023

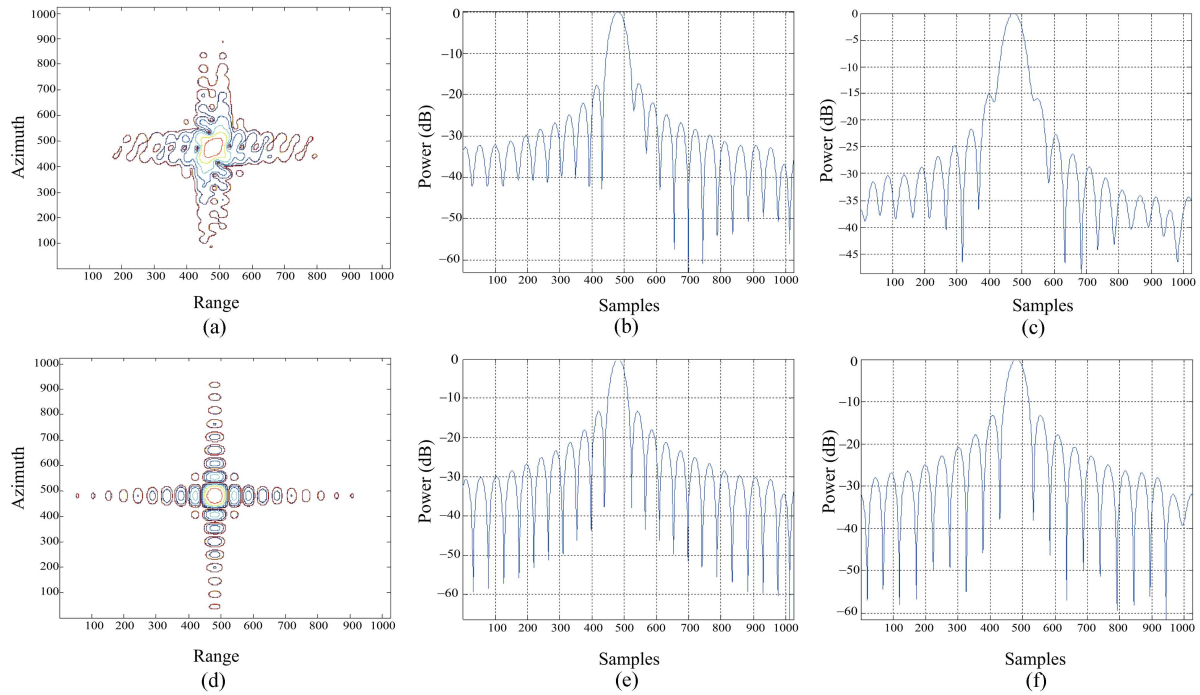


**Figure 6** (Color online) PT0 focusing result. (a) “Stop-and-go” model focusing result; (b) range slice of “stop-and-go” model; (c) azimuth slice of “stop-and-go” model; (d) “equivalent position” model focusing result; (e) range slice of “equivalent position” model; (f) azimuth slice of “equivalent position” model.

After orthogonal decomposition, the cubic power error degrades and the linear error increases. Through orthogonalization, we can also find that couplings between each power series are miniscule as shown in Figure 5(e) and (f).

After Legendre orthogonal series expansion, we can exclude the possible coupling of different power error. As a result, we can analyze the effect of each power errors on point targets focus.

## 5 Point target simulation

The error of the “stop-and-go” assumption and the feasibility of the equivalent position model were tested by point target focusing. Without the loss of generality, we chose the point target in the beam center when the true anomaly of the satellite was  $5^\circ$  and the three targets with an interval of 100 km in range direction were located in the scene, in which PT0 was at the center of the scene and PT1 was at the far end of the scene and PT2 is at the near end. The specifications of point targets are shown in Table 2.

The echo was created based on (10) and (15) then processed respectively by the parameters of the “stop-and-go” model and the equivalent position model. Using the imaging algorithm proposed in [13], the imaging results of the “stop-and-go” model and the equivalent position model are shown in Figure 6. Without losing generality, we also gave the 2-D spectrum image of the point target. The spectrum image is shown in Figure 7, which shows that the coupling of the range/azimuth is not serious owing to the attitude steering technique.

From Figure 6, we can conclude that when the synthetic aperture time reached 1000 s, the “stop-and-go” assumption lost its effect, mainly because of the quadratic slant range error.

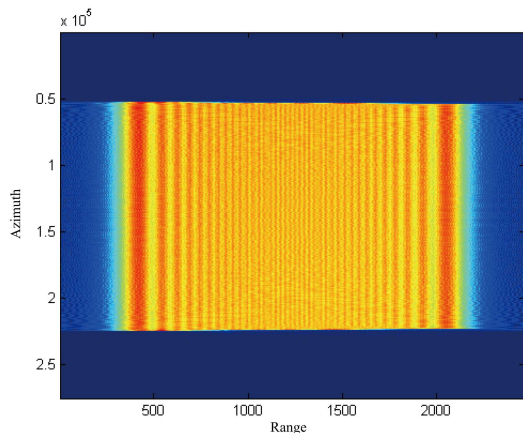


**Figure 7** (Color online) 2-dimensional spectrum of the PT0 point target.

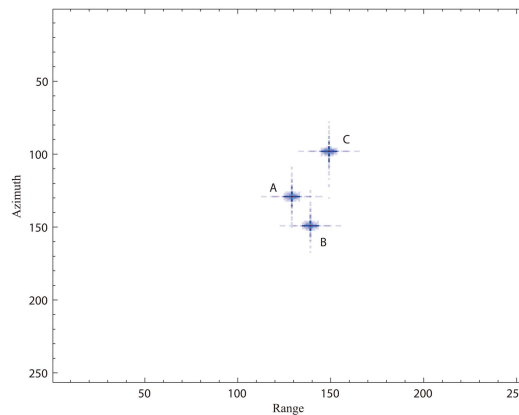


**Figure 8** (Color online) Imaging results of multi-targets with different heights.

**Table 3** Analysis on point targets

	Range			Azimuth		
	IRW (m)	PSLR (dB)	ISLR (dB)	IRW (m)	PSLR (dB)	ISLR (dB)
PT2	2.661	-13.35	-10.12	2.002	-13.27	-10.17
PT0	2.661	-13.33	-10.16	2.031	-13.26	-10.18
PT1	2.661	-13.30	-10.14	2.056	-13.23	-10.20

In order to demonstrate that our model is tolerant to the height fluctuation of the earth’s surface, we tested it with three targets of various heights. With accurate numerical calculation using the simulation parameters of Table 3, we placed targets A, B, and C on the earth with the heights of 8000 m, 4000 m, and 0 m, respectively, and the targets were in the swath of the Geo-SAR near the equator. We assumed that target A was in the center of the scene, target B was 20 m away from A, and target C was 40 m away from A and that there were no occlusions among these targets. The imaging results are shown in Figure 8. As we can see from the imaging results, the targets are well focused, which means that the height fluctuation cannot degrade the performance of our model.

## 6 Conclusion

Geo-SAR works in an orbit approximately 36000 km high, making it possible for shorter revisit times and wider swaths. However, a new imaging model and algorithm are needed to address the side effects of the increased orbit height. The “stop-and-go” assumption has been long entrenched in SAR image processing. However, owing to the unique character of Geo-SAR, the limitation of the “stop-and-go” assumption becomes obvious. As a result, it cannot be directly applied to Geo-SAR image processing when high resolution is required. In this paper, we deduce the accurate propagation delay equation of a circular orbit without any approximation. The error of the “stop-and-go” assumption and the feasibility of the equivalent position model are validated through accurate numerical calculation. Finally, a point target focusing experiment is also provided to support the above conclusion.

**Conflict of interest** The authors declare that they have no conflict of interest.

## References

- 1 Tomiyasu K, Pacelli J L. Synthetic aperture radar imaging from an inclined geosynchronous orbit. *IEEE Trans Geosci Remote Sens*, 1983, 21: 324–329
- 2 Madsen S N, Edelstein W, DiDomenico L D. A geosynchronous synthetic aperture radar for tectonic mapping, disaster management and measurements of vegetation and soil moisture. In: *Proceedings of IEEE International Conference on*

- Geoscience and Remote Sensing Symposium (IGARSS), Sydney, 2001. 447–449
- 3 Madsen S N, Chen C, Edelstein W. Radar options for global earthquake monitoring. In: Proceedings of IEEE International Conference on Geoscience and Remote Sensing Symposium (IGARSS), Toronto, 2002. 1483–1485
  - 4 Guarnieri A M, Tebaldini S, Rocca F, et al. GEMINI: geosynchronous sar for earth monitoring by interferometry and imaging. In: Proceedings of IEEE International Conference on Geoscience and Remote Sensing Symposium (IGARSS), Munich, 2012. 210–213
  - 5 Barber B C. Theory of digital imaging from orbital synthetic aperture radar. *Int J Rem Sens*, 1985, 6: 1009–1057
  - 6 Raney R K. Doppler properties of radars in circular orbits. *Intern J Remote Sens*, 1986, 7: 1153–1162
  - 7 Prats-Iraola P, Scheiber R. High precision SAR focusing of TerraSAR-X experimental staring spotlight data. In: Proceedings of IEEE International Conference on Geoscience and Remote Sensing Symposium (IGARSS), Munich, 2012: 3576–3579
  - 8 Liu Y, Xing M D, Sun G C. Echo model analysis and imaging algorithm for high-resolution SAR on high-speed platform. *IEEE Trans Geosci Remote Sens*, 2012, 50: 634–646
  - 9 Hu C, Long T, Zeng T, et al. The accurate focusing and resolution analysis method in geosynchronous SAR. *IEEE Trans Geosci Remote Sens*, 2011, 49: 634–646
  - 10 Zhao B J, Qi X Y, Song H J. The accurate fourth-order doppler parameters calculation and analysis for geosynchronous SAR. In: Proceedings of European Conference on Synthetic Aperture Radar (EUSAR), Nuremberg, 2012. 615–618
  - 11 Huang L J, Hu D H, Ding C B, et al. A general two-dimensional spectrum based on polynomial range model for medium-earth-orbit synthetic aperture radar signal processing. In: Proceedings of ICSPS, Dalian, 2010, 3: 662–665
  - 12 Huang L J. The study of Medium-earth-orbit SAR iamging algorithm. Dissertation for the Doctoral Degree. Beijing: Institute of Electronics, Chinese Academy of Sciences, 2011
  - 13 Eldhuset K. A new fourth-order processing algorithm for spaceborne SAR. *IEEE Trans Aerosp Electron Syst*, 1998, 34: 824–835